Lunar Surface Propagation Modeling Using Ray Tracing and Hardware-in-the-Loop Emulation in a Cratered Analog Environment

Nadia Kortas[1], Aaron Swank[1], Tristin Pulsipher[1], Michael Zemba[1], Nghi Tran[2]
nadia.kortas@nasa.gov
[1]NASA Glenn Research Center, USA
[2]University of Akron, USA

Keywords: 3GPP, Lunar Surface Propagation, RF Propagation Modeling, Ray-tracing Simulation, Channel Impulse Response, RF Channel Emulator

Abstract

Future lunar surface networks under NASA's Artemis program are expected to rely on terrestrial communication standards, including 3GPP New Radio (NR), to support high-data-rate applications such as enabling real-time HD video streaming and telemetry from spacesuits during Extravehicular Activity (EVA) operations and Lunar Terrain Vehicle (LTV) excursions. Although 3GPP systems are well characterized in terrestrial environments, their performance under lunar surface propagation conditions remains insufficiently understood. The lunar RF environment is dominated by extreme terrain variability, including cratered topography, and abrupt elevation changes. These conditions introduce strong diffraction, scattering, and multipath effects that significantly impact 3GPP link-level and system level performance. This work presents a measurement-driven modeling and emulation framework combining ray-tracing simulation and hardware-in-the-loop channel emulation to evaluate 3GPP performance under lunar-analog conditions. A cratered lunar-analog environment is modeled using 10-meter resolution terrain data from the Nevada National Security Site (NNSS), Icecap region. Mobility is derived from NASA JETT7 field GPS traversal data, enabling realistic line-of-sight (LOS) and non-line-of-sight (NLOS) propagation conditions. The environment captures key lunar-like features such as subsidence craters, rugged topography, and mixed terrain transitions that produce complex propagation behavior. Channel modeling is performed in Wireless InSite, where received power, path loss/gain, propagation paths, and Channel Impulse Responses (CIRs) are extracted along the measured routes, enabling detailed characterization of diffraction, reflection, and scattering in cratered terrain. The resulting CIRs are transformed into Tapped Delay Line (TDL) models and implemented on the Keysight Propsim F64 RF channel emulator for real-time hardware emulation. Results demonstrate strong alignment between simulated and field-observed propagation behavior, particularly in shadowed crater regions, validating the framework for 3GPP-based lunar surface communication system evaluation for future Artemis missions.

1 Introduction

NASA's Artemis program envisions sustained human and robotic activity on the lunar surface [1], [2], requiring architectures capable of supporting data-intensive applications such as real-time high-definition video, telemetry, and communications during EVA and LTV operations [3]. To meet these stringent reliability and capacity requirements, future lunar communication systems are expected to incorporate terrestrial wireless technologies, including Third Generation Partnership Project (3GPP) LTE and NR standards [4], [5].

While 3GPP systems are extensively characterized in terrestrial cellular deployments, their performance under lunar propagation conditions remains a critical unknown [6]. The absence of a conventional atmosphere and the extreme variability of lunar topology characterized by impact craters, ridges, and abrupt elevation changes create an RF environment dominated by severe terrain blockage, diffraction, and multipath scattering [7]. These features induce rapid transitions between LOS and NLOS states, causing profound fluctuations in signal power and delay spread over short distances.

Due to the lack of direct lunar propagation measurements, evaluating 3GPP performance requires the use of high-fidelity terrestrial analogs coupled with physics-based ray-tracing modeling [8] and hardware-in-the-loop network emulation [9], [10].

Previous work at the NASA Glenn Research Center (GRC) introduced the GRC Emulation and Modeling (GEM) testbed [11], a hardware-in-the-loop framework that couples simulated ray-traced channels with an RF channel emulator. This enables the integration of physical wireless equipment to assess the performance of terrestrial technologies, such as 3GPP and Wi-Fi, under emulated lunar surface conditions

Building upon that framework, this work presents an end-to-end, measurement-driven methodology that utilizes physical field data from the highly cratered Icecap region of NNSS. By employing these empirical field traverses to inform and calibrate the model, this methodology extracts, validates, and mathematically discretizes com-

This is a joint work of employees of the National Aeronautics and Space Administration and of the University of Akron through the Faculty Fellowship Program with the National Aeronautics and Space Administration. The United States Government may prepare derivative works, publish, or reproduce this manuscript and allow others to do so. Any publisher accepting this manuscript for publication acknowledges that the United States Government retains a non-exclusive, irrevocable, worldwide license to prepare derivative works, publish, or reproduce the published form of this manuscript, or allow others to do so, for United States government purposes.

plex lunar-analog propagation conditions into hardware-constrained Tapped Delay Line (TDL) models [12], [13] for playback in real-time hardware.

2 Lunar Analog Terrain and Field Deployment

2.1 NNSS Icecap Environment

The propagation environment utilized in this study is located in the Yucca Flat region near the planned underground nuclear test site tower Icecap at the NNSS. The site contains profound topographical features that provide a rigorous terrestrial analog for investigating wireless propagation through variable, cratered terrain similar to that found near the lunar South Pole [14]. The empirical field data utilized in this study was collected during the Joint EVA Test Team 7 (JETT7) field testing campaign in November 2024.

A digital terrain model with a spatial resolution of 10 m is used to construct the propagation environment. The terrain incorporates numerous subsidence craters, localized elevation changes, steep crater rims, and abrupt transitions between open plateaus and regions with significant terrain blockage. A visual representation of this variable subsidence crater topology, taken from the top of the Icecap tower, is provided in Figure 1. The purpose of the



Figure 1: View of the subsidence crater topology from the top of the Icecap tower at the NNSS analog testing site.

analog environment is to provide a controlled field-test setting in which terrain-driven propagation effects, specifically diffraction, multipath scattering, and deep shadowing can be measured and modeled under complex three-dimensional geometries. Figure 2 illustrates the modeled NNSS environment and the spatial locations of the two field traverses, which originated from the Icecap tower and headed southeast toward Camera Station Butte (CSB).

2.2 Field Traversal Data

Two distinct field traverses, conducted on foot, were selected for analysis because both routes navigate around

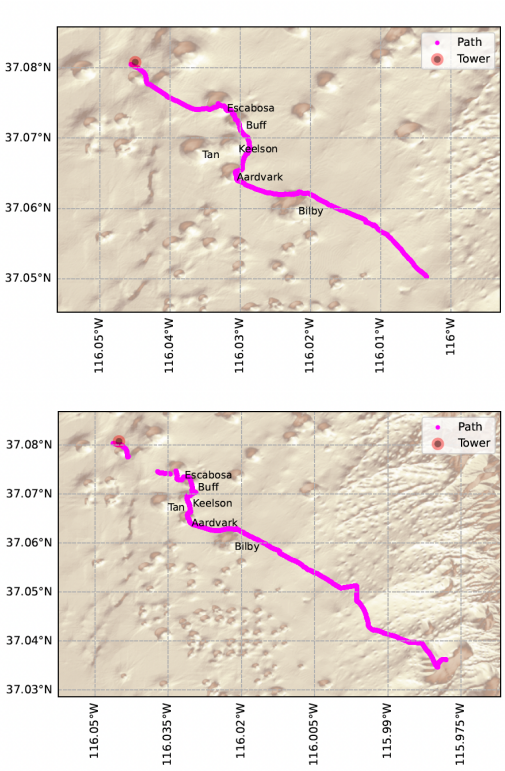


Figure 2: NNSS Icecap lunar-analog environment showing Traverse 1 (top) and Traverse 2 (bottom). [15]–[18]

and down through numerous crater features, providing substantial variation in RF propagation conditions.

- **Traverse 1 (Nov. 16, 2024):** A walking path of approximately 6 km, starting from the Icecap tower and heading southeast. The traverse navigated through several craters and concluded roughly halfway to CSB. The transmitter tower height for this traverse was configured at 15 m Above Ground Level (AGL) using an elevated lift (Figure 3).
- **Traverse 2 (Nov. 17, 2024):** An extended walking path of approximately 11 km, generally following the initial route of Traverse 1 but continuing the entire distance to CSB. To evaluate the impact of increased antenna height on diffraction over crater rims, the transmitter tower for this traverse was elevated to 30 m AGL.

For each traverse, GPS measurements were logged to capture the spatial trajectory of the mobile receiver. The GPS-measured path is subsequently mapped onto the digital terrain model to define the precise receiver locations for the ray-tracing simulations.

In addition to position data, continuous 3GPP link metrics, including Reference Signal Received Power (RSRP), were recorded. The mobile receiver configuration utilized a specially equipped backpack, shown in Figure 4. The primary metric analyzed in this study is RSRP, which corresponds to a post-mounted omnidirectional antenna located at approximately 2 m AGL to simulate an EVA



Figure 3: LTE base station positioned on an elevated lift, used to configure transmitter heights of 15 m and 30 m for the field traverses.



Figure 4: Backpack mobile receiver configuration. The primary 2 m AGL omnidirectional antenna is visible on the mast.

astronaut's helmet height. The measured RSRP provides a direct RF observation of the spatial variation in received signal strength along the routes, enabling a one-to-one empirical comparison with the simulated ray-tracing results. The primary characteristics of the two traverses are summarized in Table 1.

Table 1: Characteristics of the two cratered field traverses.

Parameter	Traverse 1	Traverse 2
Date	Nov 16, 2024	Nov 17, 2024
Traversal length	∼6 km	∼11 km
Tx tower height	15 m AGL	30 m AGL
Rx antenna height	2 m AGL	2 m AGL
Duration	216 min	268 min

2.3 Trajectory Processing

The measured GPS trajectories were processed to obtain receiver positions corresponding strictly to the propagation-modeling points. First, the geodetic trajectory was transformed into the local Cartesian coordinate system utilized by the terrain model and the ray-tracing environment.

For each receiver location, the corresponding terrain elevation was queried from the underlying US Geological Survey (USGS) digital elevation model [15]–[18]. This critical alignment step ensures that the receiver trajectory and the surrounding terrain geometry are represented consistently in the propagation simulation. Consequently, the resulting trajectory provides an accurate spatial basis for both the ray-tracing simulation and the empirical RSRP comparison, ensuring that physical crater-rim crossings and geometric terrain blockages are precisely preserved.

3 Wireless InSite Propagation Modeling

3.1 Wireless InSite Model

Propagation modeling was performed utilizing Remcom Wireless InSite [19]. The digital elevation model and receiver trajectories described in Section 2 were integrated into the three-dimensional propagation environment. The transmitter and receiver configurations were configured to replicate the exact field-test RF hardware parameters. Within the software, the digital elevation model was assigned the "Earth - Very Dry 1-100 GHz" material properties to accurately reflect the arid nature of the NNSS analog site. To ensure high-fidelity multipath calculations, the X3D propagation model was utilized and configured to allow up to 6 reflections and 1 diffraction per ray path. The simulated waveform was configured for a center frequency of 2585 MHz. During the field deployment, the baseline transmit power of the LTE base station was 5 W (37 dBm) broadcast over a 20 MHz bandwidth. To accurately evaluate the RSRP, this total power was scaled mathematically to represent the approximate power per individual subcarrier. Utilizing 12 subcarriers per Resource Block (RB) and 100 RBs for the 20 MHz band, the power was distributed across 1200 active subcarriers, yielding an intermediate subcarrier power of 6.194 dBm:

Parameter	Value
Carrier Frequency	2585 MHz
Bandwidth	20 MHz
Input Power	6.194 dBm
Material	Earth - very dry
Terrain Resolution	10 m
Ray Spacing	0.1 deg
Number of Reflections	6
Number of Diffractions	1
Tx Antenna	CIBDR Array
Tx Height	15 m, 30 m AGL
Tx Maximum Gain	10.2 dBi
Tx VSWR	1.5
Rx Antenna	Dipole
Rx Height	2 m AGL
Rx Threshold	-150 dBm
Rx VSWR	2.5

Table 2: Wireless InSite Configuration Settings

$$P_{\text{subcarrier}} = 10\log_{10}\left(\frac{5000\text{ mW}}{1200\text{ subcarriers}}\right) \approx 6.194\,\text{dBm}. \tag{1}$$

The physical base station utilized a cross-polarized ($\pm 45°$) antenna array oriented at a 64° azimuth from true north. Because the mobile receiver utilized a vertically polarized (0°) omnidirectional antenna, a 3 dB polarization mismatch loss was inherent to the physical link. To account for this hardware mismatch, 3 dB polarization loss factor was subtracted from the computed propagation results.

The transmit and receive antenna radiation patterns were explicitly defined in the simulation using `.uan` files. The base station transmitter was modeled using a Collinear Inverse Biconical Dipole Array (CIBDR), custom-designed for lunar surface applications, exhibiting a maximum gain of 10.2 dBi. The mobile receiver was modeled using a standard dipole pattern sourced from the Ansys HFSS antenna toolkit [20], yielding an omnidirectional gain of 3.0 dBi. Based on manufacturer data sheet parameters, the Voltage Standing Wave Ratio (VSWR) was configured to 2.5 and 1.5 for the transmitter and receiver antennas respectively. The configuration steps are summarized in Figures 5 and 6, and the principal simulation parameters are detailed in Table 2.

At each discrete spatial receiver position, Wireless InSite calculates the individual propagation paths comprising the received signal and natively generates the corresponding time-varying CIR. This direct software output encapsulates the complex amplitudes and delays of all valid multipath components. This site-specific modeling approach permits the characterization of rapidly fluctuating propagation mechanisms, an essential requirement when modeling highly irregular, cratered terrain.

3.2 LOS and NLOS Propagation

The digital terrain geometry is utilized to identify critical transitions between LOS and NLOS conditions. When direct visibility between the transmitter and receiver is obstructed by terrain, the receiver's link relies entirely on diffracted, reflected, or scattered components. The distinction between LOS and NLOS regions provides a framework for interpreting variations in both received power and channel multipath structure. Specifically, crater rims and steep inclines obstruct the direct path, creating localized regions of severe signal attenuation. Concurrently, this loss of the dominant LOS path induces substantial delay spread as the receiver is forced to rely on delayed environmental reflections to sustain the link.

Figures 7 and 8 explicitly illustrate this geometric cause-and-effect relationship for the two traverses. The vertically aligned panels demonstrate how physical descent into craters (Traverse 1) or ascents along steep terrain features like CSB (Traverse 2) directly trigger NLOS conditions. These terrain-induced blockages coincide flawlessly with severe drop-offs in received power and immediate spikes in RMS delay spread, directly motivating the necessity of hardware channel emulation to evaluate system performance in such highly dispersive environments.

3.3 Channel Impulse Response

For each spatial receiver position, the ray-tracing simulation outputs a discrete set of propagation components characterized by complex amplitude and propagation delay. The corresponding CIR is represented as

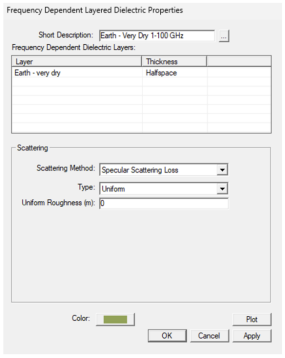
$$h(t) = \sum_{k=1}^{K} a_k e^{j\phi_k}\delta(t-\tau_k), \tag{2}$$

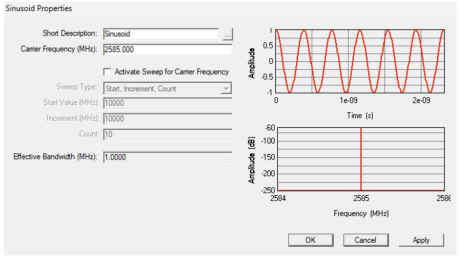
where K is the number of valid propagation paths, a_k is the magnitude of the k-th component, ϕ_k is its relative phase, and τ_k is its physical Time of Arrival (TOA) delay.

The resulting CIR provides critical spatial intelligence beyond aggregate received power. As evidenced by the RMS delay spread analysis in the preceding section, the distribution of propagation delays and phase amplitudes serves as the fundamental basis for characterizing the frequency-selective fading structure produced by the cratered topology. To evaluate 3GPP performance within this environment, these raw CIRs must be mathematically discretized for ingestion by real-time hardware channel emulators.

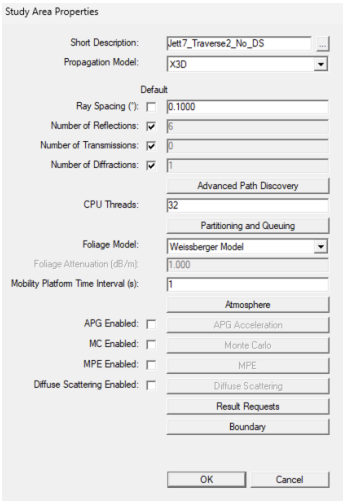
4 Field Measurement and Propagation Results

The JETT7 field measurements provide the primary empirical reference for evaluating the Wireless InSite (WI) propagation model. For each traverse, the measured RSRP, obtained using the 2 m AGL omnidirectional antenna, is compared with the WI-predicted received power. The measured GPS trajectory and discrete WI receiver

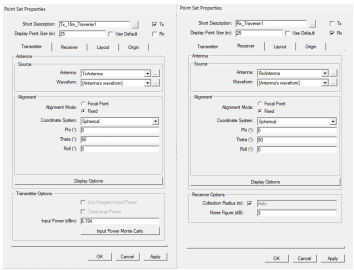




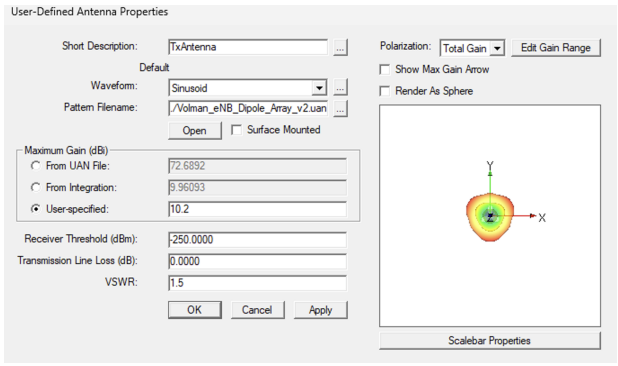
(a) Material & Waveform



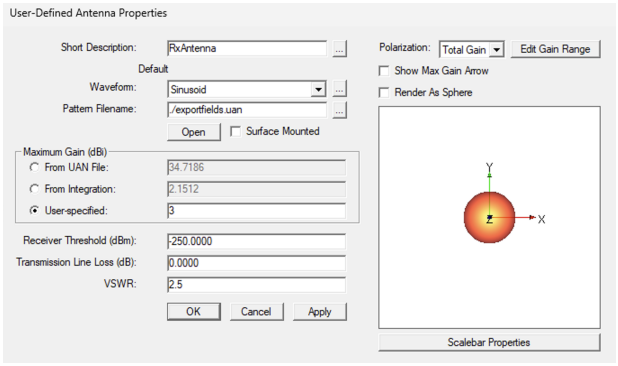
(b) Study Area (X3D)



(c) Tx and Rx Setup



(d) Tx Antenna (10.2 dBi)



(e) Rx Antenna (3.0 dBi)

Figure 5: Overview of the Wireless InSite project configuration.

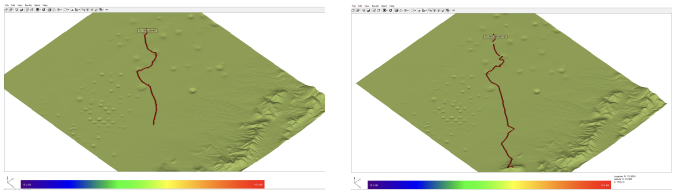


Figure 6: 3D project views in Wireless InSite displaying Traverse 1 (15 m Tx, left) and Traverse 2 (30 m Tx, right) routed through the imported digital elevation model of the cratered terrain.

locations are mapped to a common normalized traverse coordinate so that both datasets are compared over the same physical terrain regions.

4.1 Measured and Simulated Received Power

The spatial comparison evaluates both the overall received-power trend and the locations of terrain-induced signal attenuation. Agreement in the locations of major signal reductions provides an indication of whether the ray-tracing model captures the dominant terrain-driven propagation transitions. For each WI receiver location, the total received power is calculated by summing all returned propagation components in linear power:

$$P_{\mathrm{sim},i} = 10\log_{10}\left(\sum_{k=1}^{N_i} 10^{P_{i,k}/10}\right), \tag{3}$$

where $P_{i,k}$ is the received power of propagation path k in dBm and N_i is the number of returned paths.

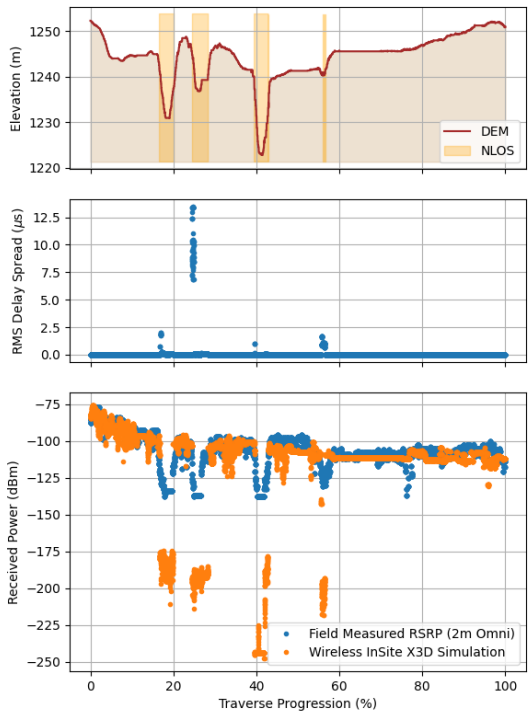


Figure 7: Propagation analysis for Traverse 1 using the 15 m tower. The subplots depict physical terrain elevation with LOS/NLOS state (top), the resulting RMS delay spread (middle), and the field-measured RSRP vs. Wireless InSite simulated received power (bottom).

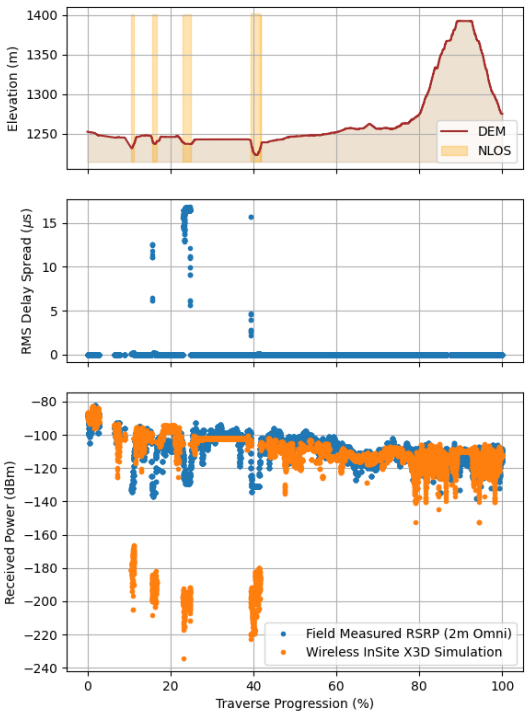


Figure 8: Propagation analysis for Traverse 2 using the 30 m tower. The subplots depict physical terrain elevation with LOS/NLOS state (top), the resulting RMS delay spread (middle), and the field-measured RSRP vs. Wireless InSite simulated received power (bottom).

The mean error and root-mean-square error (RMSE) are calculated as:

$$E_{\text{mean}} = \frac{1}{M}\sum_{i=1}^{M}\left(P_{\text{sim},i} - P_{\text{meas},i}\right), \tag{4}$$

$$\text{RMSE} = \sqrt{\frac{1}{M}\sum_{i=1}^{M}\left(P_{\text{sim},i} - P_{\text{meas},i}\right)^2}, \tag{5}$$

where M is the number of valid paired samples.

4.1.1 Traverse 1: Figure 7 compares the measured and simulated received-power profiles along Traverse 1 using the 15 m transmitter.

The major signal reductions occur at similar spatial locations in the measured and simulated profiles, including prominent transitions near approximately 35%, 45%, and 60% of the traverse. This agreement indicates that the ray-tracing model captures the principal terrain-induced LOS/NLOS transitions. The comparison yields a mean error of −5.66 dB and an RMSE of 38.19 dB. The relatively small mean error indicates limited overall bias, while the larger RMSE reflects localized discrepancies in terrain-obstructed regions. The current WI version has a known diffraction-modeling limitation that can overestimate diffracted energy in complex terrain. This limitation is expected to be addressed in a future software release and may contribute to discrepancies in strongly obstructed regions.

4.1.2 Traverse 2: Figure 8 shows the corresponding comparison for Traverse 2. Major spatial variations occur near approximately 7%, 20%, and 38% of the normalized traverse. The comparison yields a mean error of 3.77 dB and an RMSE of 23.77 dB. The relatively small mean error indicates limited overall bias, while the RMSE reflects localized discrepancies in complex terrain. These results are also subject to the diffraction-modeling limitation of the current WI version discussed above.

4.2 Statistical Received-Power Variation

To compare received-power variation independently of the absolute power level, each dataset is median-normalized:

$$F_{\text{dB},i} = P_{\text{rx},i} - \widetilde{P}_{\text{rx}}, \tag{6}$$

where $\widetilde{P}_{\text{rx}}$ is the median of all valid received-power samples over the complete traverse. Positive and negative values therefore represent constructive and destructive variations in the channel response, respectively.

4.2.1 Traverse 1: Figure 9 compares the CDF of the median-normalized fading for the field measurements and WI simulation.

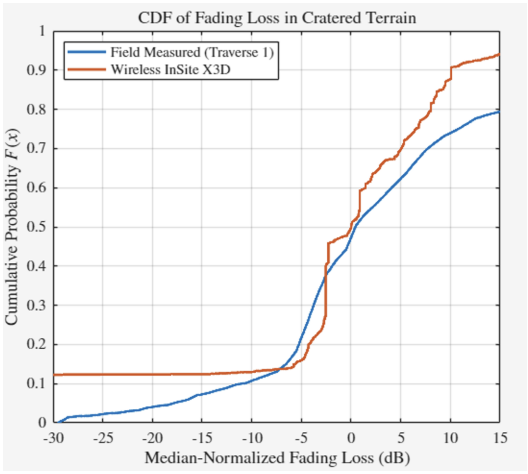


Figure 9: CDF of median-normalized fading along Traverse 1 for the field measurements and Wireless InSite simulation.

The simulated and measured distributions show similar behavior over the primary fading region, indicating that the WI model captures the dominant statistical effects of terrain-induced multipath interference. Differences in the tails are associated primarily with the strongest shadowing and constructive-interference events.

4.2.2 Traverse 2: The corresponding fading distribution for Traverse 2 is shown in Figure 10.

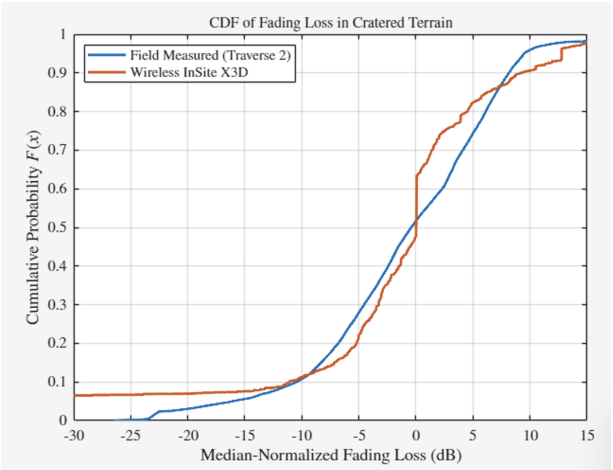


Figure 10: CDF of median-normalized fading along Traverse 2 for the field measurements and Wireless InSite simulation.

The measured and simulated distributions exhibit similar behavior in the central multipath-fading region, despite differences in transmitter height, traverse length, and terrain geometry. The consistency across both traverses supports the use of WI for characterizing terrain-induced fading in the lunar-analog environment.

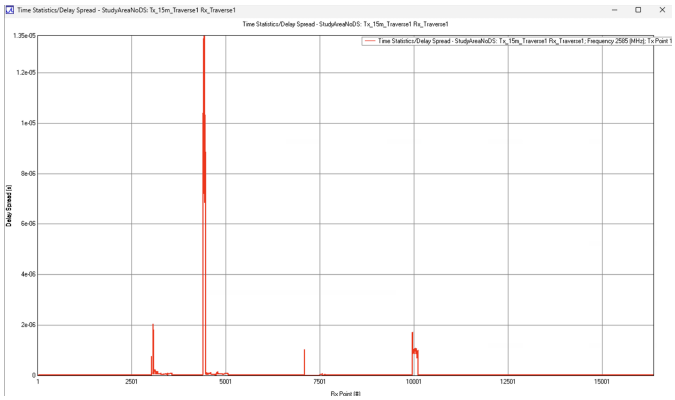


Figure 11: RMS delay spread across Traverse 1 generated by Wireless InSite at 2585 MHz. The traversal shows repeated transitions between clear LOS (near-zero delay spread) and highly dispersive NLOS environments.

4.3 Propagation Through Cratered Terrain

The traverses contain repeated transitions between clear LOS and terrain-obstructed propagation. To evaluate these effects, channel characteristics were simulated in Wireless InSite (WI) using a single carrier frequency of 2585 MHz. When the direct path is blocked by crater terrain, reflected and diffracted components can become more significant, producing increased temporal dispersion. The RMS delay spread, which characterizes the spread of the total transit time of arrival of all multipath signals, is calculated from the WI propagation components as:

$$\tau_{\mathrm{RMS}} = \sqrt{\overline{\tau^2} - (\overline{\tau})^2}, \tag{7}$$

where the power-weighted first and second delay moments are:

$$\overline{\tau} = \frac{\sum_k P_k \tau_k}{\sum_k P_k}, \qquad \overline{\tau^2} = \frac{\sum_k P_k \tau_k^2}{\sum_k P_k}. \tag{8}$$

Here, P_k is the linear power of propagation component k and τ_k is its propagation delay.

Analysis of the RMS delay spread across Traverse 1 generated by WI (Fig. 11) reveals distinct regions of NLOS propagation, characterized by two distinct classes of multipath behavior: macro-delays from distant terrain and micro-delays from local crater geometry. The most extreme macro-delays occur as the receiver enters the second crater near Rx Point 4415, exhibiting RMS spreads reaching 13.5 μs, corresponding to extra propagation distances of over 4 km. These originate from reflections off distant geographical features, such as the mountain peaks to the East of the traversal area (visualized in Fig. 12, Top). To evaluate the potential impact on the OFDM waveform, the RMS delay spread is evaluated against the symbol period. Dividing the 13.5 μs delay spread by the standard LTE symbol period of 66.67 μs yields a ratio of approximately 0.2. Because this ratio exceeds the general threshold of 0.1, the channel is expected to exhibit severe frequency-selective fading. Indeed, because the primary LOS path is heavily attenuated by the crater terrain, it is

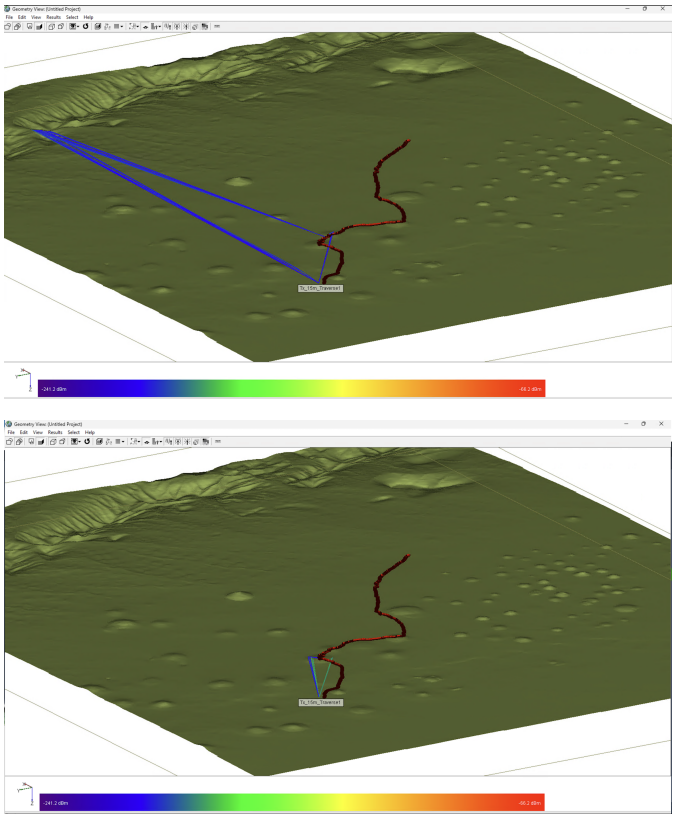


Figure 12: Wireless InSite 3D ray-tracing visualizations illustrating distinct multipath environments during the traverse. (Top) Macro-delays originating from distant mountain reflections near Rx Point 4415. (Bottom) Localized micro-delays reflecting off the immediate Escabosa crater walls near Rx Point 3063.

forced to compete with both the delayed macro-reflections and concurrent local reflections. This complex superposition vastly exceeds the standard LTE normal cyclic prefix (CP) of approximately 4.7 μs potentially introducing inter-symbol interference (ISI) and actively degrades the link through severe frequency-selective fading. Examining the delay spread profile during shallower NLOS events, specifically along the edges of the Escabosa crater near Rx Point 3063, reveals dense clusters of micro-delays ranging from 250 ns up to 2 μs. This temporal spread corresponds to excess path lengths of 75 m to 600 m, perfectly aligning with localized reflections off the immediate and opposing crater walls (visualized in Fig. 12, Bottom). Because these specific delays fall well within the LTE CP, they do not cause ISI; instead, they combine to induce deep frequency-selective fading nulls across the OFDM subcarriers. From a mission planning perspective, it is this localized, sub-CP multipath that heavily governs the degradation of the wireless link inside the crater environments. These highly dispersive regions provide the representative multipath conditions used for the subsequent hardware channel emulation.

5 Wireless InSite CIR-to-TDL Conversion

5.1 Hardware Emulation Constraints and OMP Formulation

To enable hardware-in-the-loop (HWIL) replay of the Wireless InSite (WI) channel realizations, the continuous-delay multipath data generated by the ray-tracing model needs to be converted into a discrete TDL representation compatible with the PROPSIM F64 channel emulator [11]. The converter is configured for a 20 MHz LTE waveform using $N_{\text{used}} = 1200$ active subcarriers with a $\Delta f = 15$-kHz subcarrier spacing, corresponding to an 18-MHz occupied subcarrier span. The hardware TDL representation uses a nominal 5-ns delay-grid resolution and up to $L_{\max} = 48$ complex taps per channel realization.

In multicarrier systems such as 4G LTE or 5G NR, link performance is governed primarily by the channel transfer function across the active subcarriers rather than conventional delay-domain moments. As such, an accurate hardware emulation must prioritize preserving the frequency response over the occupied signal bandwidth. Specifically, each subcarrier n experiences a complex channel gain $H_{\text{WI}}(f_n)$ at baseband frequency $f_n = \left(n - 1 - \frac{N_{\text{used}}-1}{2}\right)\Delta f, \quad n = 1, \ldots, N_{\text{used}}$. Here, $H_{\text{WI}}(f)$ is the channel frequency response (CFR), which is the Fourier transform of the CIR $h(t)$, and it can be written as:

$$H_{\text{WI}}(f) = \sum_{k=1}^{K} a_k e^{j\phi_k} e^{-j2\pi f \tau_k}. \tag{9}$$

Note that for each snapshot, rays falling more than 60 dB below the dominant path can be discarded; these components carry negligible energy and have no noticeable effect on $H_{\text{WI}}(f)$. Because a hardware TDL profile is defined by L discrete taps with propagation delays $\{\tau_\ell\}_{\ell=1}^{L}$ and complex gains $\{g_\ell\}_{\ell=1}^{L}$, the synthesized channel frequency response is $H_{\text{TDL}}(f) = \sum_{\ell=1}^{L} g_\ell e^{-j2\pi f \tau_\ell}$. To best match $H_{\text{TDL}}(f)$ to the true channel response $H_{\text{WI}}(f)$ across the active subcarriers, the tap parameters are chosen to minimize the in-band squared error. The tap fitting problem can therefore be formulated as a joint optimization of tap gains and tap delays as:

$$\min_{L,\{\tau_\ell\},\{g_\ell\}} \sum_{n=1}^{N_{\text{used}}} \left| \sum_{\ell=1}^{L} g_\ell e^{-j2\pi f_n \tau_\ell} - H_{\text{WI}}(f_n) \right|^2, \tag{10}$$

subject to the hardware budget $L \le L_{\max} = 48$ and grid constraints $\tau_\ell \in \{m d_{\text{hw}}\}$.

This optimization problem corresponds to a non-convex harmonic-retrieval problem characterized by numerous local minima [21]. When the delays are restricted to the 5-ns emulator grid, the problem simplifies to choosing at most $L_{\max} = 48$ grid positions and finding their complex gains to best match $H_{\text{WI}}(f_n)$ [13]. Although finding the optimal subset of delay positions is combinatorial, it can be solved efficiently using greedy pursuit methods. Specifically, we

Inputs:

$\boldsymbol{Rays}_{N_{\text{CIRs}}}$	Wireless InSite multipath ray sets for each CIR snapshot
$N_{\text{used}} = 1200,\ \Delta f = 15\,\text{kHz}$	Number and spacing of utilized subcarriers
$d_{\text{hw}} = 5\,\text{ns}$	PROPSIM hardware delay-grid spacing
$\tau_{\max} = 5.12\,\mu\text{s}$	Maximum local ray-delay window
$\Delta P_{\max} = 60\,\text{dB}$	Ray power window relative to the peak ray
$L_{\max} = 48$	Maximum number of PROPSIM taps

Outputs:

$\boldsymbol{Coeff}_{L_{\max}\times N_{\text{CIRs}}}$	Normalized complex tap gains
$\boldsymbol{Delay}_{L_{\max}\times N_{\text{CIRs}}}$	Global-reference tap delays in nanoseconds

Algorithm:

1.	$\tau_{\min,\text{global}} \leftarrow \min_{s,r} \tau_{s,r}$	Determine the minimum ray delay across all CIR snapshots.
2.	**For each snapshot** s	Process each Wireless InSite CIR independently.
3.	$\tau_{\min,s} \leftarrow \min_r \tau_{s,r}$	Determine the earliest ray delay in the current snapshot.
4.	$\mathcal{R}_s \leftarrow \{r : P_{s,r} \geq P_{s,\max} - \Delta P_{\max},\ \tau_{s,r} - \tau_{\min,s} \leq \tau_{\max}\}$	Retain rays within the 60-dB power window and 5.12-μs local-delay window.
5.	$\tau^{\text{rel}}_{s,r} \leftarrow \tau_{s,r} - \tau_{\min,s}$	Express retained ray delays relative to the snapshot minimum.
6.	$a_{s,r} \leftarrow 10^{P_{s,r}/20} e^{j\phi_{s,r}}$	Convert ray power and phase to complex amplitudes.
7.	$\boldsymbol{f}_{sc} \leftarrow \left(n - \frac{N_{\text{used}}-1}{2}\right)\Delta f$	Construct the centered subcarrier-frequency vector.
8.	$\tau_{\text{cand,max}} \leftarrow \max_r \tau^{\text{rel}}_{s,r} + 50\,\text{ns}$	Set the OMP dictionary limit using the maximum retained local delay plus a 50-ns margin.
9.	$\mathcal{D} \leftarrow \{kd_{\text{hw}} : k = 0, \ldots, \lfloor \tau_{\text{cand,max}}/d_{\text{hw}} \rfloor\}$	Construct the PROPSIM-aligned candidate delay dictionary.
10.	$\boldsymbol{h} \leftarrow \boldsymbol{A}_{\text{ray}}\boldsymbol{a}, \quad [\boldsymbol{A}_{\text{ray}}]_{n,r} = e^{-j2\pi f_n \tau^{\text{rel}}_r}$	Compute the exact Wireless InSite frequency response.
11.	$\boldsymbol{r} \leftarrow \boldsymbol{h}, \quad \Omega \leftarrow \varnothing$	Initialize the OMP residual and selected-delay set.
12.	$\omega^\star \leftarrow \arg\max_{\omega\in\mathcal{D}\setminus\Omega} \lvert \boldsymbol{a}_\omega^H \boldsymbol{r}\rvert$	Select the candidate delay having maximum correlation with the residual.
13.	$\Omega \leftarrow \Omega \cup \{\omega^\star\}$	Add the selected delay and prevent its reselection.
14.	$\boldsymbol{g}_\Omega \leftarrow \boldsymbol{A}_\Omega^\dagger \boldsymbol{h}$	Re-estimate the selected complex gains using the truncated-SVD pseudoinverse with relative singular-value threshold $\text{rtol} = 10^{-3}$.
15.	$\boldsymbol{r} \leftarrow \boldsymbol{h} - \boldsymbol{A}_\Omega \boldsymbol{g}_\Omega$	Update the frequency-domain residual.
16.	$\rho \leftarrow \lVert\boldsymbol{r}\rVert_2 / \lVert\boldsymbol{h}\rVert_2$	Compute the normalized residual.
17.	**Repeat Steps 12–16**	Continue until $\lvert\Omega\rvert = L_{\max}$ or $\rho \leq \text{tol}_{\text{res}}$.
18.	$\Omega, \boldsymbol{g}_\Omega \leftarrow \text{sort}(\Omega, \boldsymbol{g}_\Omega)$	Sort the selected delays and corresponding gains in ascending delay order.
19.	$\tau^{\text{local}} \leftarrow \Omega d_{\text{hw}}$	Convert selected dictionary indices to local delays on the 5-ns hardware grid.
20.	$\Delta\tau_s \leftarrow \tau_{\min,s} - \tau_{\min,\text{global}}$	Determine the continuous snapshot bulk shift relative to the global minimum delay.
21.	$\tau^{\text{global}} \leftarrow \tau^{\text{local}} + \Delta\tau_s$	Restore the snapshot-to-snapshot propagation-delay variation without rounding the bulk shift.
22.	$\boldsymbol{g} \leftarrow \boldsymbol{g}_\Omega / \max\lvert\boldsymbol{g}_\Omega\rvert$	Normalize the selected gains by their maximum magnitude.
23.	$\boldsymbol{Coeff}[:, s] \leftarrow \boldsymbol{g}, \quad \boldsymbol{Delay}[:, s] \leftarrow 10^9 \tau^{\text{global}}$	Store the normalized gains and global-reference delays; zero-pad unused tap entries to $L_{\max}$.
24.	**End For**	Repeat for all CIR snapshots.

Figure 13: Wireless InSite CIR-to-PROPSIM conversion using frequency-domain Orthogonal Matching Pursuit. The ray delays are first referenced to the minimum delay of each snapshot for OMP fitting. The OMP candidate delays are defined on the PROPSIM 5-ns grid, while the continuous snapshot bulk shift relative to the global minimum delay is restored after OMP processing.

consider an orthogonal matching pursuit (OMP)-based approximation [22]–[24] as we describe in the following.

First, the fitting target is represented as the vector $\mathbf{h} = [H_{\text{WI}}(f_1), \ldots, H_{\text{WI}}(f_{N_{\text{used}}})]^T \in \mathbb{C}^{N_{\text{used}}}$. Each candidate delay τ_m has a known in-band frequency signature $\mathbf{a}_m \in \mathbb{C}^{N_{\text{used}}}$ with entries:

$$(\mathbf{a}_m)_n = e^{-j2\pi f_n \tau_m}, \quad n = 1, \ldots, N_{\text{used}}. \tag{11}$$

Note that every candidate signature has equal energy, i.e., $\|\mathbf{a}_m\|^2 = N_{\text{used}}$. Instead of attempting to solve for all tap locations and gains simultaneously, OMP iteratively selects one tap at a time. At any iteration, suppose our

current model leaves an unexplained residual error $\mathbf{r}$ (with $\mathbf{r}_0 = \mathbf{h}$ initially). When evaluating an individual candidate tap at delay τ_m, its contribution in band is $g\mathbf{a}_m$. To absorb as much residual energy as possible, we choose its gain to minimize the leftover error:

$$\min_g \|\mathbf{r} - g\mathbf{a}_m\|^2. \tag{12}$$

This is a single-column least-squares problem with the closed-form solution:

$$g_{\text{opt}} = \frac{\mathbf{a}_m^H \mathbf{r}}{\|\mathbf{a}_m\|^2}. \tag{13}$$

The energy removed by adding this tap is $|\mathbf{a}_m^H \mathbf{r}|^2 / \|\mathbf{a}_m\|^2$. Because all columns have the same norm, the candidate that absorbs the most energy is simply the one whose frequency signature correlates most strongly with the residual.

Writing $\mathcal{S}_t$ for the set of selected tap delays after t iterations, the algorithm proceeds as follows:

1. *Select the Best Match:* Identify the candidate delay that maximizes the correlation with the current residual, and add it to the active support:

$$m_t = \arg\max_{m \notin \mathcal{S}_{t-1}} \left|\mathbf{a}_m^H \mathbf{r}_{t-1}\right|, \qquad \mathcal{S}_t = \mathcal{S}_{t-1} \cup \{m_t\}. \tag{14}$$

2. *Re-fit Gains on the Selected Support:* With the tap delays fixed to the active set $\mathcal{S}_t$, solving for the complex gains of the selected taps is a linear least-squares problem with closed-form solution:

$$\mathbf{g}_t = \mathbf{A}_{\mathcal{S}_t}^{+} \mathbf{h}, \tag{15}$$

   where $\mathbf{A}_{\mathcal{S}_t}$ contains only the columns corresponding to the selected support $\mathcal{S}_t$. Because adjacent taps on a 5-ns grid can produce nearly collinear columns over an 18-MHz span, $\mathbf{A}_{\mathcal{S}_t}^{+}$ is evaluated using a truncated-SVD pseudoinverse with a relative threshold of $\varrho = 10^{-3}$ to ensure numerical stability.

3. *Update Residual:* Compute the new residual error:

$$\mathbf{r}_t = \mathbf{h} - \mathbf{A}_{\mathcal{S}_t} \mathbf{g}_t. \tag{16}$$

   Because $\mathbf{g}_t$ is the least-squares solution on $\mathcal{S}_t$, the residual $\mathbf{r}_t$ is orthogonal to all selected columns, ensuring no redundant tap reselection.

This process repeats until reaching the 48-tap budget or until the residual error becomes negligible. In practice, setting the residual tolerance to zero allows the algorithm to use the full 48-tap budget, deploying low-power corrective taps across adjacent bins to equalize continuous off-grid delay arrivals. The overall conversion procedure was implemented as a custom Python processing pipeline, as summarized in Fig. 13.

5.2 Time-of-Flight Preservation and Tap Normalization

Preservation of the modeled propagation time-of-flight is achieved by separating the local multipath representation from the snapshot-dependent bulk propagation delay. The OMP optimization is performed using relative delays referenced to the minimum delay of each snapshot. After the OMP coefficients are obtained, the continuous bulk offset is restored relative to the global minimum delay across the complete trajectory:

$$\tau_{\text{bulk},s} = \tau_{s,\min} - \tau_{\text{global,min}} \tag{17}$$

and the final delay associated with each selected tap is:

$$\tau_{s,m} = \tau_{s,m}^{\text{local}} + \tau_{\text{bulk},s}. \tag{18}$$

The current implementation preserves this bulk offset as a continuous value; it is not rounded to the 5-ns hardware grid. Consequently, the local multipath structure is represented on the hardware delay grid while the snapshot-to-snapshot propagation-delay evolution is retained through the continuous bulk-delay offset.

Following the OMP solution, tap coefficients are normalized independently for each snapshot by the magnitude of the strongest selected coefficient. This establishes a 0-dB reference for the strongest tap while preserving the relative magnitude and phase relationships of the remaining taps. The normalization is applied after the frequency-domain reconstruction error is evaluated and therefore does not alter the reported OMP reconstruction accuracy. By normalizing the coefficients, the algorithm maximizes the dynamic range of the emulator's small-scale fading engine. However, this removes the large-scale path loss caused by the lunar terrain, meaning the overall signal attenuation must be computed and applied to the emulator as a separate shadowing profile.

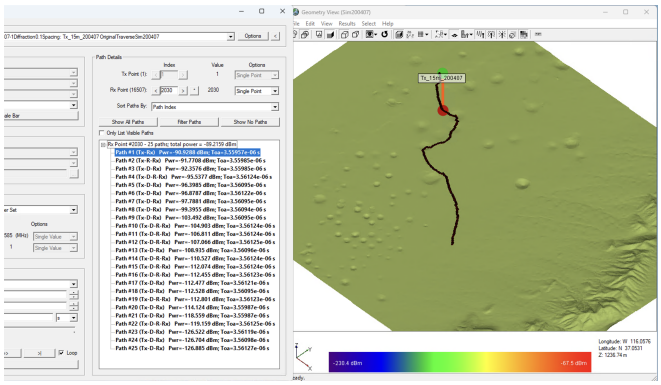
5.3 CIR Conversion Assessment

The accuracy of the TDL conversion is evaluated by comparing the exact WI frequency response with the response reconstructed from the OMP-selected taps. The normalized mean-square error (NMSE) is calculated as:

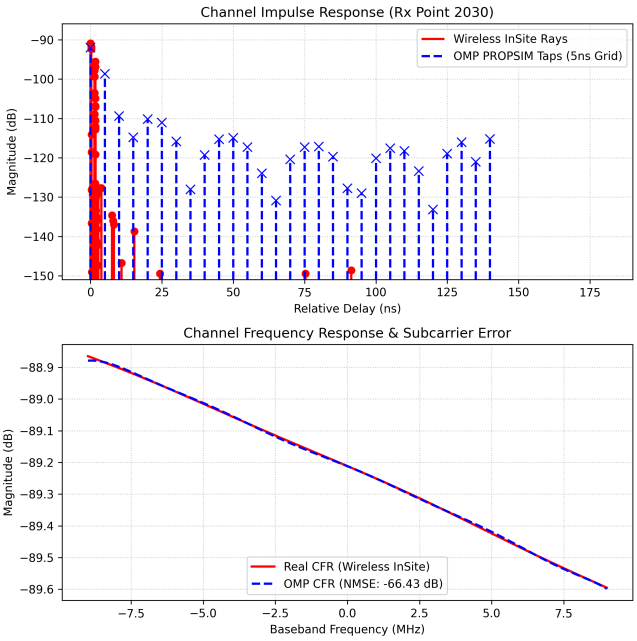
$$\text{NMSE}_{\text{dB}} = 10 \log_{10} \left(\frac{\sum_{n=1}^{N_{\text{used}}} |H_{\text{WI}}(f_n) - H_{\text{TDL}}(f_n)|^2}{\sum_{n=1}^{N_{\text{used}}} |H_{\text{WI}}(f_n)|^2} \right). \tag{19}$$

To validate the robustness of the OMP conversion algorithm, a segment of the traversal descending into the first major crater of Traverse 1 (Rx Points 2000 to 5500) was analyzed. Figures 14 and 15 illustrate the physical 3D ray-tracing paths alongside their corresponding frequency-domain reconstructions at four critical trajectory points in this segment.

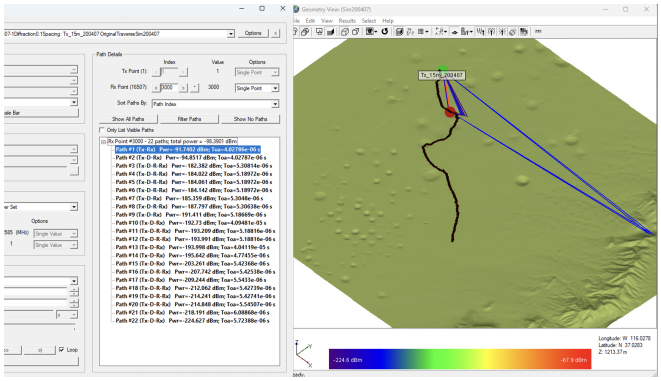
When the receiver experiences clear LOS conditions (e.g., Rx 2030), the physical propagation is dominated by a strong initial path, resulting in relatively flat frequency fading. Under these conditions, the OMP algorithm successfully maps the channel to the 5 ns emulator grid with NMSE values routinely below -66 dB.



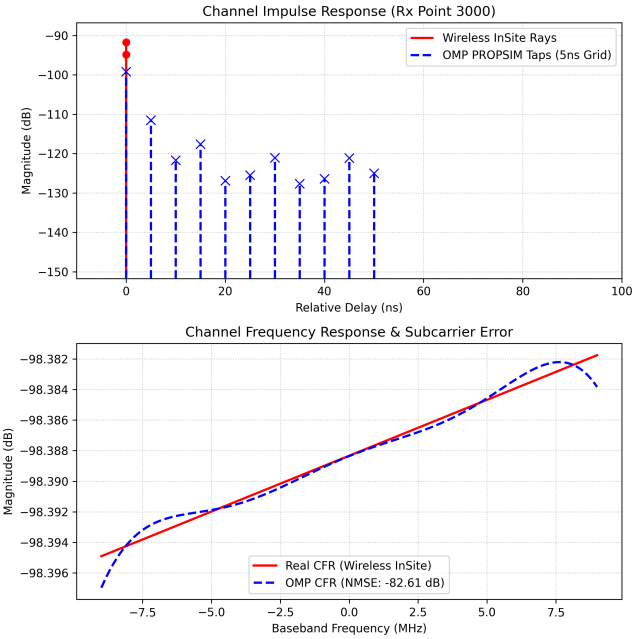
(a) Rx 2030: 3D Ray-Tracing Paths



(b) Rx 2030: OMP TDL Reconstruction



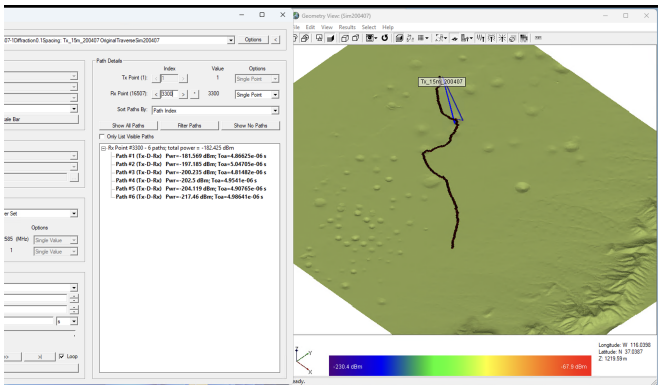
(c) Rx 3000: 3D Ray-Tracing Paths



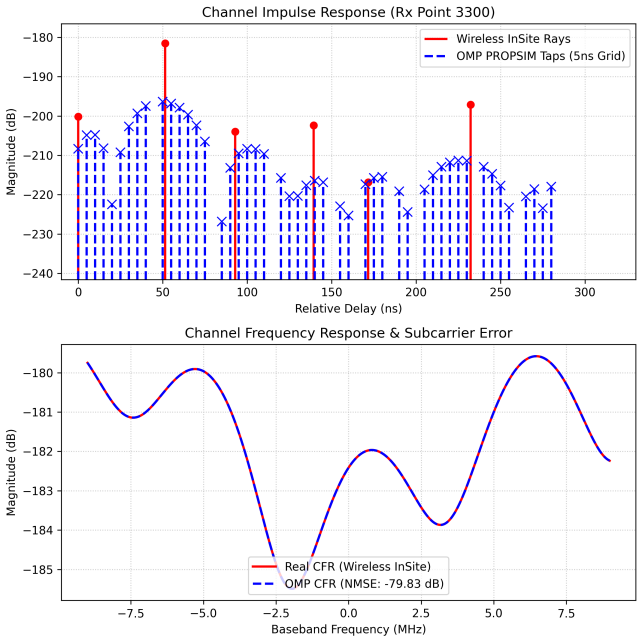
(d) Rx 3000: OMP TDL Reconstruction

Figure 14: Channel state evolution (Part 1). Pre-crater LOS propagation (Rx 2030) and crater-edge propagation (Rx 3000). The left column shows the Wireless InSite ray-tracing paths, while the right column shows the corresponding hardware-constrained frequency-domain OMP reconstruction.

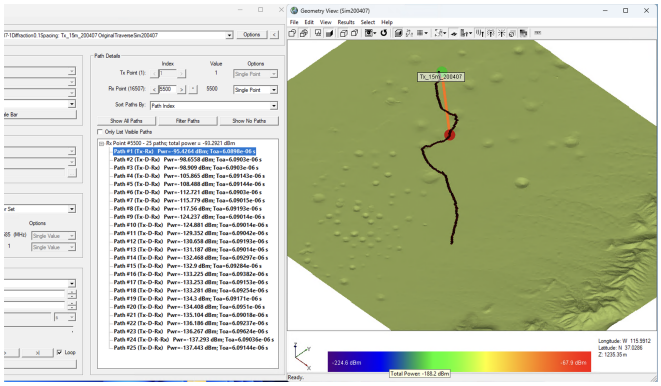
As the receiver descends into the first crater (e.g., Rx 3300), it enters the severe NLOS environment where the direct path is entirely blocked by the crater rim. The CIR becomes heavily dispersed by the localized crater reflections discussed in Section , inducing deep frequency-selective fading nulls. Finally, when the receiver emerges from the crater (e.g., Rx 5500), the dominant LOS path is restored returning the channel to a flat fading regime. Notably, the OMP algorithm frequently generates a higher density of discrete emulator taps than original continuous ray paths to model these conditions. This is a mathematical necessity of the hardware constraint; to accurately re-



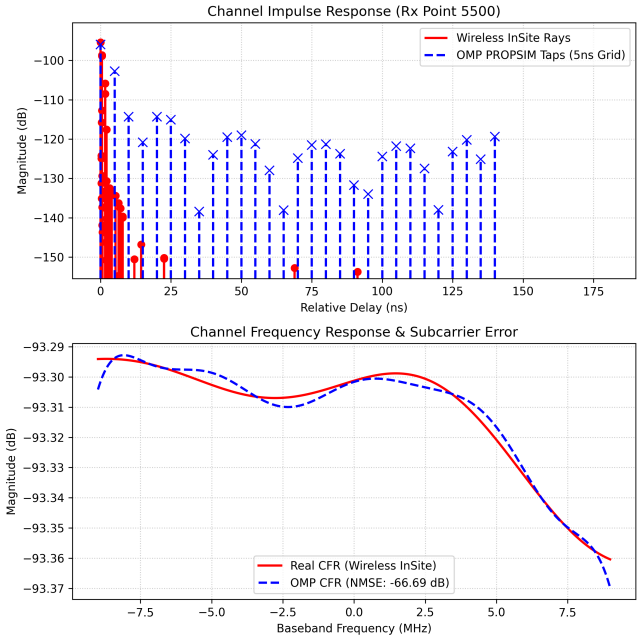
(a) Rx 3300: 3D Ray-Tracing Paths



(b) Rx 3300: OMP TDL Reconstruction



(c) Rx 5500: 3D Ray-Tracing Paths



(d) Rx 5500: OMP TDL Reconstruction

Figure 15: Channel state evolution (Part 2). Deep-crater NLOS propagation (Rx 3300) is followed by recovery of the dominant LOS component after exiting the crater (Rx 5500).

construct an off-grid continuous delay (e.g., 12.5 ns), the algorithm distributes complex weights across multiple adjacent 5 ns hardware grid points. By utilizing its full allocation of 48 taps and deploying low-power corrective taps to act as a frequency-domain equalizer, the algorithm faithfully reproduces the exact frequency-selective fading profile caused by the local crater walls, driving the residual CFR error down even in highly dispersive crater environment.

In addition to localized micro-delays, the OMP converter must also successfully reproduce fading environments induced by extreme macro-delays. As the receiver enters the second crater near Rx Point 4415, the primary LOS path is severely attenuated (dropping below

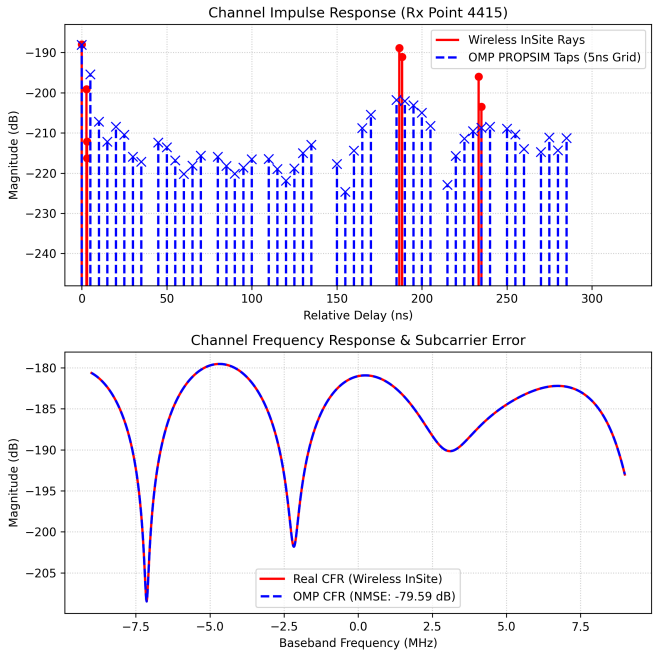


Figure 16: OMP TDL Reconstruction at Rx Point 4415. The deep frequency-selective fading nulls are successfully captured as the heavily attenuated direct path competes with macro-delays from distant terrain.

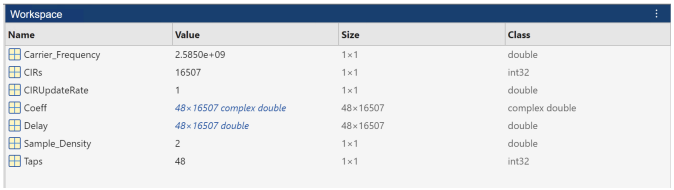


Figure 17: Traverse 1 MATLAB workspace output generated by the OMP converter, detailing the structured arrays required by the PROPSIM hardware emulator.

−188 dB), forcing it to actively compete with delayed macro-reflections arriving roughly 200 ns later. As illustrated in Fig. 16, this temporal interference produces severe, wideband fading nulls separated by approximately 5 MHz in the frequency domain. Despite the complexity of these fades, the OMP algorithm successfully places discrete taps on the 5 ns hardware grid to capture the exact channel frequency response, maintaining an excellent NMSE of nearly −80 dB. Finally, when the receiver completely emerges from the cratered terrain (e.g., Rx 5500), the dominant LOS path is restored, returning the channel to a predictable flat fading regime.

5.4 Hardware Emulation File Generation

Following conversion of all channel snapshots, the normalized complex coefficients and reconstructed delays are assembled into the final TDL representation. For the configured 48-tap case, the coefficient and delay arrays have dimensions

$$\mathbf{C} \in \mathbb{C}^{48\times N_{\mathrm{CIR}}}, \qquad \mathbf{D} \in \mathbb{R}^{48\times N_{\mathrm{CIR}}}, \tag{20}$$

where each column corresponds to one WI channel snapshot and each row corresponds to one TDL tap. Tap locations not selected by OMP are zero-filled.

The resulting data are written to a MATLAB-compatible workspace containing the carrier frequency, complex TDL coefficients, delays, CIR update-rate parameter, sample-density parameter, and configured tap count. Because the TDL coefficients in the MATLAB workspace are normalized per snapshot, the large-scale path loss and shadowing variations, such as the severe signal attenuation experienced when descending into a crater, must be applied independently. To achieve this, the converter computes the total filtered ray energy for each snapshot directly from the Wireless InSite outputs. A relative large-scale attenuation profile is then generated by referencing each snapshot's total energy to the maximum valid energy observed over the entire traversal. This macroscopic path loss is exported as a separate PROPSIM shadowing file (`.shd`), which provides the emulator with the sequential attenuation values needed to scale the normalized tap coefficients across the trajectory. This dual-file representation provides the interface between the WI propagation model and subsequent PROPSIM F64 hardware-in-the-loop channel emulation, enabling the modeled lunar propagation environment to be replayed as a time-varying, frequency-selective channel.

6 Hardware-in-the-Loop Emulation

6.1 GEM Hardware Testbed Integration

To evaluate the operational impact of the modeled lunar terrain on end-to-end network performance, the discrete TDL channel models derived in Section 5 were deployed in a physical Hardware-in-the-Loop (HWIL) configuration. The Keysight PROPSIM F64 RF channel emulator was integrated directly with the 3GPP communications hardware utilized in the NASA GEM testbed, as illustrated in Figure 18.

The testbed utilizes the srsRAN 4G software radio suite operating on USRP N310 hardware to replicate the base station (eNodeB and Evolved Packet Core) and User Equipment (UE) protocol stacks. By inserting the PROPSIM into the RF path between the eNodeB and the UE, the configuration enables direct observation of the impact of simulated crater-induced fading on communications-system performance at the physical, MAC, and application layers. The PROPSIM was configured to update the emulated channel conditions at 1 Hz, matching the temporal sampling of the channel snapshots used in the traverse.

During the emulation, application-layer performance was evaluated using two distinct Uplink (UL) traffic profiles transmitted from the UE to the eNodeB: a continuous UDP traffic stream generated using the `iperf` network

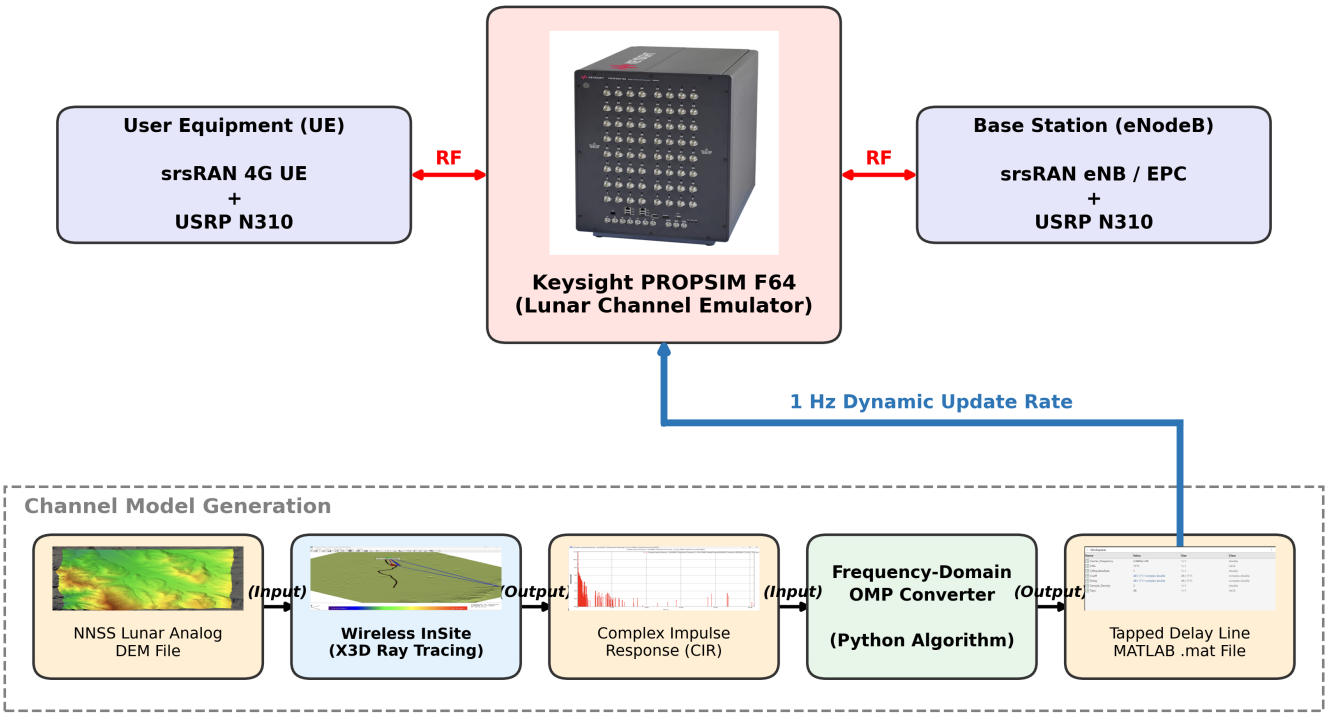


Figure 18: Hardware-in-the-loop test configuration (GEM testbed). The discrete TDL channels generated from the Wireless InSite CIRs are ingested by the PROPSIM F64, which emulates the crater-induced fading between the 3GPP base station and UE hardware.

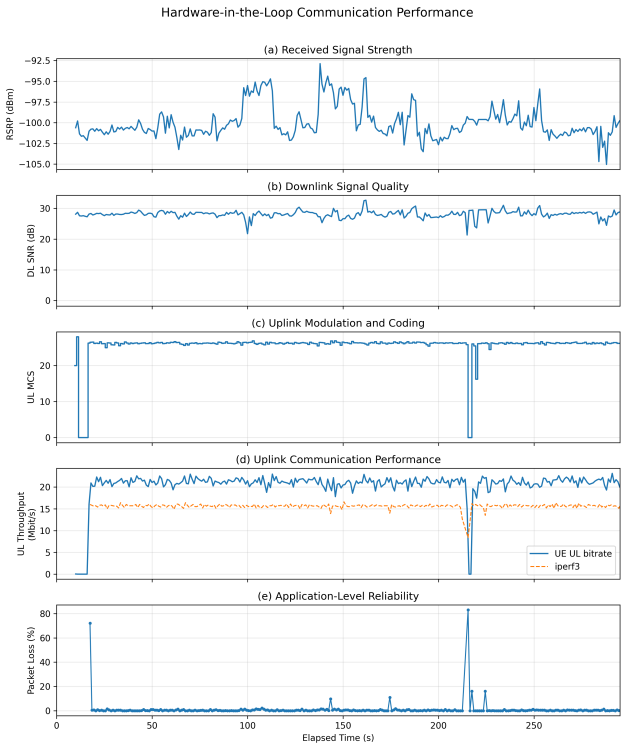


Figure 19: Representative 3GPP hardware-in-the-loop performance during Traverse 1. As the emulated channel enters a crater region, the severe reduction in RSRP is accompanied by degradation of the uplink link adaptation, resulting in a reduction in uplink throughput and increased packet loss.

testing utility and a 4K video streaming profile representing high-definition EVA helmet-camera feeds.

Because the experiment focused on the UE-to-eNodeB uplink path, diagnostic logs were recorded at the eNodeB to characterize the resulting link performance. Uplink data throughput was used as the primary application-layer performance metric to evaluate link stability and quantify the impact of the modeled propagation conditions on user-data delivery. Additional physical and MAC layer metrics, including RSRP, SNR, and UL MCS, were recorded to correlate changes in propagation conditions with link-adaptation behavior and application-layer performance.

6.2 3GPP Performance Under Crater-Induced Propagation

The HWIL emulation results establish a direct relationship between the propagation characteristics identified in Section 4 and end-to-end communications-system performance. Figure 19 presents synchronized time-series measurements from the 3GPP hardware as it experiences the dynamic propagation conditions derived from Traverse 1. By synchronizing physical and MAC layer diagnostic metrics with the application-layer measurements, the resulting degradation in communications performance can be observed during severe propagation events.

As shown in Figure 19, at approximately 215 seconds of elapsed time, the simulated receiver enters the crater region, resulting in a reduction in RSRP(Panel a), consistent with the loss of the dominant LOS component. The Downlink Signal-to-Noise Ratio (SNR) (Panel b) remains relatively stable under the controlled noise conditions of the emulation. Because the HWIL experiment evaluated a UE-to-eNodeB uplink traffic path, the resulting degradation is observed directly in the uplink link adaptation and application layer performance metrics.

As the channel enters the severe fading region, the Uplink Modulation and Coding Scheme (UL MCS) abruptly drops to zero (Panel c), indicating that the uplink can no longer sustain normal link adaptation. This MAC-layer degradation directly translates to application-level impairments. Panel (d) shows the corresponding reduction in the reported UE uplink bitrate and measured `iperf` throughput, which collapse to zero during the most severe portion of the fading event. This degradation coincides with a substantial increase in packet loss (Panel e). Continuous video streaming could therefore not be sustained during the severe channel impairments associated with the simulated crater region.

As the simulated receiver emerges from the deepest portion of the fading geometry, the channel recovers toward a LOS condition. The uplink link adaptation subsequently recovers, restoring the MCS and allowing the uplink throughput to return toward its nominal level. These results demonstrate that the discrete 48-tap TDL channel models derived from lunar-analog ray-tracing simulations can be integrated into a physical 3GPP HWIL environment to reproduce dynamic propagation conditions and evaluate their impact on end-to-end communications performance.

7 Acknowledgement

This work was supported by the National Aeronautics and Space Administration (NASA) Space Communications and Navigation (SCaN) program in the Research and Technology Mission Directorate (RTMD) with additional funding from the NASA Glenn Faculty Fellowship Program (NGFFP).

8 Conclusion

This paper presented a measurement-driven framework for modeling and emulating wireless propagation in a cratered lunar-analog environment to support future NASA Artemis missions. The end-to-end methodology successfully combined empirical field measurements, site-specific Wireless InSite ray-tracing simulations over high-resolution terrain, mathematical CIR-to-TDL conversion, and PROPSIM F64 Hardware-in-the-Loop testing using an open-source 3GPP software radio stack.

Two field traverses through the highly cratered NNSS Icecap region were analyzed. The measured GPS trajectories were incorporated into the three-dimensional propagation model, providing realistic, spatially varying receiver dynamics. The robust alignment between the field-measured RSRP and the simulated ray-tracing results validated the capacity of the geometric model to predict macroscopic path loss and the geographic onset of severe propagation voids. Furthermore, the ray-tracing simulations provided critical insight into the underlying physical mechanisms, specifically crater-rim diffraction and multipath scattering, that dictate channel performance during LOS-to-NLOS transitions.

A critical contribution of this work was the formulation, implementation and validation of an OMP algorithm to mathematically transform the continuous Wireless InSite CIRs into discrete TDL representations. This conversion provided an accurate practical bridge between site-specific propagation simulation and real-time, hardware-constrained emulation. The resulting HWIL architecture enabled direct observation of critical 3GPP system vulnerabilities, demonstrating how crater-induced signal degradation immediately throttles Uplink application layer throughput and disrupts high-definition 4K video streaming transfers.

While the NNSS environment serves as a terrestrial analog and does not encapsulate all absolute physical properties of the lunar surface, the results demonstrate that field-informed ray tracing combined with HWIL emulation provides a rigorous, repeatable framework for investigating terrain-dependent telecom performance. Future work will refine the ray-tracing diffuse scattering models, extend the analysis to dynamic LTV mobility scenarios and incorporate empirical channel sounding measurements planned for the upcoming NASA JETT8 field campaign.

Furthermore, the HWIL testbed will be upgraded to evaluate 3GPP 5G NR standards and used to further quantifying the relationship between specific crater geometries and QoS margins.

9 References

[1] S. Creech *et al.*, "Artemis: An overview of nasa's activities to return humans to the moon," in *IEEE Aerospace Conference*, Big Sky, MT, USA, 2022.

[2] National Aeronautics and Space Administration, "Moon to mars objectives," Tech. Rep., 2022.

[3] K. Coggins *et al.*, "Nasa's approach to lunar communication and navigation: Artemis and beyond," in *75th International Astronautical Congress (IAC)*, Milan, Italy, 2024.

[4] B. Edwards *et al.*, "3gpp mobile telecommunications technology on the moon," in *IEEE Aerospace Conference*, Big Sky, MT, USA, 2023, pp. 1–12.

[5] 3GPP, "Study on new radio (nr) to support non-terrestrial networks," 3rd Generation Partnership Project (3GPP), Technical Report TR 38.811, 2020.

[6] V. Badescu *et al.*, "Lunar surface communication: Rf propagation and network topology," *IEEE Aerospace and Electronic Systems Magazine*, vol. 30, no. 5, pp. 16–25, 2015.

[7] K. L. Smith and D. Michelson, "Ray-tracing analysis of lunar surface rf propagation in cratered terrain," in *IEEE Aerospace Conference*, 2021, pp. 1–10.

[8] Z. Yun and M. F. Iskander, "Ray tracing for radio propagation modeling: Principles and applications," *IEEE Access*, vol. 3, pp. 1089–1100, 2015.

[9] L. Bonati *et al.*, "Colosseum: Large-scale wireless experimentation through hardware-in-the-loop network emulation," in *IEEE International Symposium on Dynamic Spectrum Access Networks (DySPAN)*, Los Angeles, CA, USA, 2021, pp. 105–113.

[10] O. Kodheli *et al.*, "5g space communications lab: Reaching new heights," in *18th International Conference on Distributed Computing in Sensor Systems (DCOSS)*, Marina del Rey, CA, USA, 2022, pp. 349–356.

[11] M. Hilts, T. Pulsipher, L. Leslie, M. Zemba, and A. J. Swank, "Emulation testbed for the development of lunar surface communication systems," in *Proceedings of the Ka and Broadband Communications Conference*, NASA Glenn Research Center, 2024.

[12] A. W. Mbugua *et al.*, "On simplification of ray tracing channels in radio channel emulators for device testing," in *15th European Conference on Antennas and Propagation (EuCAP)*, Dusseldorf, Germany, 2021, pp. 1–5.

[13] A. W. Mbugua *et al.*, "Efficient preprocessing of site-specific radio channels for virtual drive testing in hardware emulators," *IEEE Transactions on Aerospace and Electronic Systems*, vol. 59, no. 2, pp. 1787–1799, 2023.

[14] M. O'Connor *et al.*, *Lunar lro nac haworth photoclinometry dem 1m*, `https://astrogeology.usgs.gov/search/map/lunar_lro_nac_haworth_photoclinometry_dem_1m`, Accessed: August 8, 2025.

[15] U.S. Geological Survey, *USGS 1/3 arc second n37w116 20250113*, 2025.

[16] U.S. Geological Survey, *USGS 1/3 arc second n37w117 20130101*, 2013.

[17] U.S. Geological Survey, *USGS 1/3 arc second n38w116 20250115*, 2025.

[18] U.S. Geological Survey, *USGS 1/3 arc second n38w117 20241206*, 2024.

[19] Remcom Inc., *Wireless InSite 3d wireless prediction software*, `https://www.remcom.com/wireless-insite-propagation-software`, 2024.

[20] Ansys Inc., *Ansys HFSS: 3d high frequency simulation software*, `https://ansys.synopsys.com/products/electronics/ansys-hfss`, 2026.

[21] P. Stoica and R. Moses, *Spectral analysis of signal*, Upper Saddle River, NJ, USA: Prentice Hall, 2005.

[22] S.G.Mallat and Z.Zhang, "Matching pursuits with time-frequency dictionaries," *IEEE Trans. Signal Process*, vol. 41, no. 12, pp. 3397–3415, 1993.

[23] R. Y. C.Pati and P. S.Krishnaprasad, "Orthogonal matching pursuit: Recursive function approximation with applications to wavelet decomposition," *Proc. 27th Asilomar Conf. Signals, Syst. Comput.*, pp. 40–44, 1993.

[24] J.A.Tropp and A.C.Gilbert, "Signal recovery from random measurements via orthogonal matching pursuit," *IEEE Trans. Inf. Theory*, vol. 53, no. 12, pp. 4655–4666, 2007.